ACS APPLIED ENERGY MATERIALS

www.acsaem.org Article

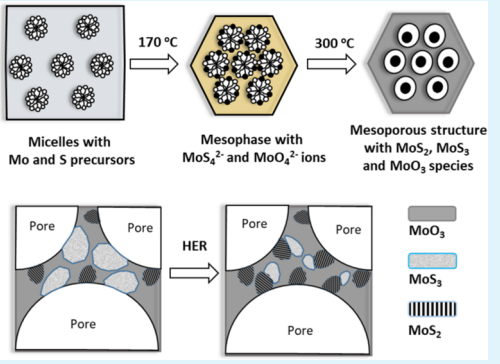
Mesoporous Molybdenum Sulfide-Oxide Composite Thin-Film Electrodes Prepared by a Soft Templating Method for the Hydrogen Evolution Reaction

Cüneyt Karakaya, Navid Solati, Timuçin Balkan, Umut Savacı, Emre Keleş, Servet Turan, and Sarp Kaya*

Cite This: *ACS Appl. Energy Mater.* 2022, 5, 7006−7015 Read Online

ACCESS | Metrics & More | Article Recommendations | Supporting Information

ABSTRACT: Electrode designs involving binder-free nanoparticles integrated within interconnected pore networks are critical in scaling up electrolyzers. MoS_2 is the most promising electrocatalyst candidate that can show hydrogen evolution reaction (HER) activity comparable to platinum (Pt). Herein, a facile one-step soft templating method was developed to synthesize mesoporous molybdenum sulfide-oxide composite thin-film electrocatalysts directly on any substrate without using a binder or a template. Fabricated electrocatalysts contain amorphous MoS_3 and small crystallite-sized MoS_2 embedded into amorphous MoO_3 with a large surface area (around 182 m^2/g). The electrocatalyst layer undergoes in situ electrochemical activation in which amorphous MoS_3 is reduced to MoS_2 during the HER in acidic media. The electrocatalyst layer on the carbon fiber exhibits a low overpotential (~189 mV at 10 mA/cm^2) and Tafel slope (53 mV/dec) toward the HER after electrochemical activation.



KEYWORDS: *MoS_2, mesoporosity, hydrogen evolution, cathode, soft-templated growth*

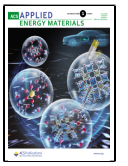
INTRODUCTION

With the continuously decreasing renewable electricity cost, the production of green hydrogen has been increasingly becoming economically attractive and has turned out to be a critical key to reach the net-zero target.[1] To achieve this, electrolyzers with almost 5000 GW of power must be deployed by 2050.[2] Therefore, all technical and economic barriers to electrolysis technologies must be overcome to make electrolyzers viable for widespread implementation. The efforts involve minimizing the kinetic losses on both anodes and cathodes, where the oxygen evolution reaction (OER) and the hydrogen evolution reaction (HER) take place, respectively.

Platinum (Pt) is the best electrocatalyst for the HER; however, its large-scale application is limited due to its high cost and low abundance.[3] MoS_2, a significant member of two-dimensional (2D) transition-metal dichalcogenides, has been used as a hydrodesulfurization catalyst in the petroleum refinery industry for decades due to its abundant, inexpensive, and reversible hydrogen desorption properties.[4] It has also exhibited strong electrochemical activity, and it has been shown by theoretical calculations that S-terminated edge sites of MoS_2 might be active for the HER,[5] which has later been confirmed experimentally.[6] S-terminated edge sites are active, whereas the basal planes and Mo-terminated edges, which comprise the majority of the sites, are inert for the HER.[6] The relative activities of edge sites, vacancies, and grain boundaries of MoS_2 have been determined by Tafel analysis, and the slopes have been calculated to be 65−75 mV/dec for edge sites, 65−85 mV/dec for sulfur vacancies, and 120−160 mV/dec for grain boundaries.[7]

One strategy for elevating the HER activity is to generate an amorphous catalyst because a disordered atomic orientation may induce more electrochemically active sites.[8] However, amorphous MoS_3 has been shown to undergo a structural transformation toward MoS_2 under HER conditions.[9] Operando ambient-pressure X-ray photoelectron spectroscopy (APXPS) has been used to demonstrate the conversion from MoS_3 to MoS_2, Mo 3d and S 2p spectral changes under negative bias show progressive compositional change and put forward MoS_2 phase critical for enhanced HER activity.[10] Further evidence for structural modification has been provided by in situ transmission electron microscopy (TEM). Amorphous MoS_2 simultaneously crystallizes under negative bias.[11]

Received: March 1, 2022
Accepted: May 23, 2022
Published: June 7, 2022



© 2022 The Authors. Published by American Chemical Society

Downloaded from pubs.acs.org/aaemcq/article-pdf/5/6/7006/4453682/ae2c00640.pdf by KOC UNIV user on 29 October 2026

2D layered structures lack the electrical conductivity required for electrochemical applications owing to the weak electronic coupling between van der Waals layers. The electrocatalytic activity of a single layer MoS_2 for the HER decreases with the addition of a second layer, adding the potential barrier of 0.119 V.[12] The nanostructured crystalline MoS_2 is very useful in terms of accelerating the mass transfer, improving electron conductivity, and avoiding restacking.[13] Therefore, many nanostructured MoS_2-based electrocatalysts, i.e., hierarchical structures,[14] quantum dots,[15] micro-nano spheres,[16] and flowerlike nanoflakes,[17] were designed, synthesized, and tested for the HER.

Application of catalyst ink from 2D materials is troublesome due to restacking of the layers after solvent evaporation.[18] Three-dimensional (3D) structures of nanostructured MoS_2 with an interconnected conductive network are crucial to prevent restacking and provide a high specific surface area with improved conductivity.[19] For this reason, carbon-based support materials such as carbon nanofibers,[20,21] carbon cloths,[22−24] carbon papers,[25] carbon nanotubes,[26] and graphene foams[27] have been used. For example, W-doped MoS_2 and MoO_2 heterostructures on carbon nanotubes exhibit Pt-like HER activity.[28] The more conductive MoO_2 bridges the less conductive MoS_2, and the carbon matrix facilitates the charge transport between MoS_2 and carbon nanotubes. Doping high valance atom, W, into the MoS_2 lattice also activates the basal plane S atoms and results in an enhanced HER activity. Another strategy to boost the HER activity is to activate the basal planes of MoS_2 by creating sulfur vacancies.[29−32] The concentration of sulfur vacancies that maximizes the HER performance is between 12.5 and 15.62%.[32]

The porous electrocatalysts provide better mass transport and are beneficial for large-scale electrocatalyst fabrications. The high porosity potentially increases the surface area, which further leads to the exposure of abundant internal sulfur-terminated edge sites. For this reason, mesoporous transition-metal sulfides have attracted great attention owing to their superior performance as catalysts, electrodes, and photocatalytic materials.[33−40] The hard templating method has been applied for the synthesis of mesoporous metal sulfides such as FeS_2, CoS_2, NiS_2, WS_2, and MoS_2.[41,42] There are several examples of mesoporous MoS_2 thin films prepared using this method,[43] whereas the synthesis of mesoporous metal sulfides by soft templating is still very challenging due to the uncontrollable fast precipitation process between metal salts and the S_2^- ions. Mesoporous iron-doped $MoS_2/CoMo_2S_4$ powder electrocatalyst that shows superior HER activity in alkaline media has been developed.[44] However, the synthesis of mesoporous MoS_2 thin-film electrocatalysts via the soft templating route remains challenging.

The one-step production protocol enabling the formation of 3D integrated porous structures without a postcoating process does not require nonconductive organic binders and offers a robust alternative for efficient electrode preparation. The stable lyotropic liquid mesophase with two surfactants and various transition-metal nitrates has been converted to mesoporous $MnCo_2O_4$, $NiCo_2O_4$ $LiMn_2O_4$, $ZnCo_2O_4$, and NiO thin films for many applications.[45−48] The same strategy has been adopted to prepare mesoporous NiS_2 electrodes for the HER.[49] Mesoporous MoS_2 thin-film electrodes are ideal for improved mass transfer and the number of HER active sites. To the best of our knowledge, a one-step method that enables mesoporous MoS_2 thin-film coating with narrow pore sizes for the HER has not been developed. Herein, we modified the liquid crystalline templating strategy to obtain mesoporous MoS_2 thin-film electrodes for the HER. In addition, we showed the applicability and scalability of this method by preparing larger electrodes (5 cm × 5 cm) on commercial substrates like carbon cloth.

EXPERIMENTAL SECTION

Preparation of Solutions of Molybdenum and Sulfur Precursor and Surfactants. In a typical solution preparation, cetyltrimethylammonium bromide (CTAB), polyoxyethylene (10) lauryl ether ($C_{12}EO_{10}$), ammonium heptamolybdate tetrahydrate ($(NH_4)_6Mo_7O_{24}{\cdot}4H_2O$), and thiourea ($CH_4N_2S$) were mixed in a 25 mL vial with deionized water. Later, the ammonia solution (NH_4OH) was added dropwise via a pipette. When ethylene glycol ($C_2H_6O_2$) was used for the preparation of the solution, it was added before the addition of the ammonia solution. The solution is stirred for 1 day to make sure that it is homogeneous and clear (transparent and colorless). A schematic representation of the general solution preparation is shown in Figure S1. Amounts of each ingredient for the solution with/without ethylene glycol are tabulated in Tables S1 and S2, respectively.

Preparation of Lyotropic Liquid Crystalline (LLC) Mesophase. Ingredients of the solution used for preparing mesophases are given in Tables S1 and S2 for thin LLC films. Spin coating was used to prepare LLC and further mesoporous MoS_2 thin films. A few drops of the solution were placed on the FTO or microscopic glass, and it was spun for 20 s at 1000 rpm by a spin coater. To obtain a thicker mesophase, drop-cast coating on the microscopic slides was also applied. Drop-casting was applied by placing a few drops of solutions and aged for evaporation of deionized water. Schematic representations of both drop-cast and spin coating methods are shown in Figure S2.

Preparation of Mesoporous MoS_2 on FTO. The mesoporous MoS_2 electrodes, synthesized by adopting liquid crystalline templating on a flat conductive substrate (fluorine-doped tin oxide (FTO) coated glass), were used for the HER. Before spin coating, FTO substrates (1 cm × 2 cm) were cleaned by ultrasonication in absolute ethanol. The electrodes were prepared by spin coating from the clear solutions with the corresponding composition. A Scotch tape was used to make an area of 1 cm^2 on the FTO for spin coating. The mesophase film over the FTO was annealed at 170 and 300 °C in a nitrogen (N_2) atmosphere for 1 and 2 h, respectively. The as-prepared samples were also further annealed at 400 and 500 °C for 2 h. The electrodes were used for electrochemical measurements and also for the analysis like XPS, scanning electron microscopy (SEM), energy-dispersive X-ray spectroscopy (EDX), etc. Schematic representations of the preparation of electrodes are given in Figure S3.

Preparation of Mesoporous MoS_2 on Carbon Fiber. Before spin coating, carbon fibers were cleaned by ultrasonication in absolute ethanol. The carbon fibers were cut into pieces having sizes of 0.1 cm × 2 cm. Half of it was dipped into the clear solutions. The carbon fibers were placed on the glass substrate and then spin-coated at 1000 rpm for 20 s. The mesophase film over the carbon fiber was annealed at 170 and 300 °C in a nitrogen (N_2) atmosphere for 1 and 2 h, respectively. Schematic representations of the preparation of electrodes are presented in Figure S4.

Preparation of Mesoporous MoS_2 on Carbon Cloth with a Microporous Layer. The commercial carbon cloth with a microporous layer (CeTech W1S1009-FuelCellStore) was cut into 5 cm × 5 cm pieces. The cut piece was placed on a larger glass substrate, and then the mesophase was prepared by spin-coating the solution at 1000 rpm for 20 s on the microporous side (Figure S5). The mesophase coating was annealed at 170 and 300 °C in a nitrogen (N_2) atmosphere for 1 and 2 h, respectively.

Instrumentation. Powder X-ray diffraction (XRD) measurements were performed at room temperature on a Bruker D-8 diffractometer (Cu Kα radiation, λ = 1.5406 Å). A beam voltage of 40 kV and a current of 40 mA were used. The phase identification of the patterns

Downloaded from pubs.acs.org/aaemcq/article-pdf/5/6/7006/4453682/ae2c00640.pdf by KOC UNIV user on 29 October 2026

https://doi.org/10.1021/acsaem.2c00640
ACS Appl. Energy Mater. 2022, 5, 7006−7015

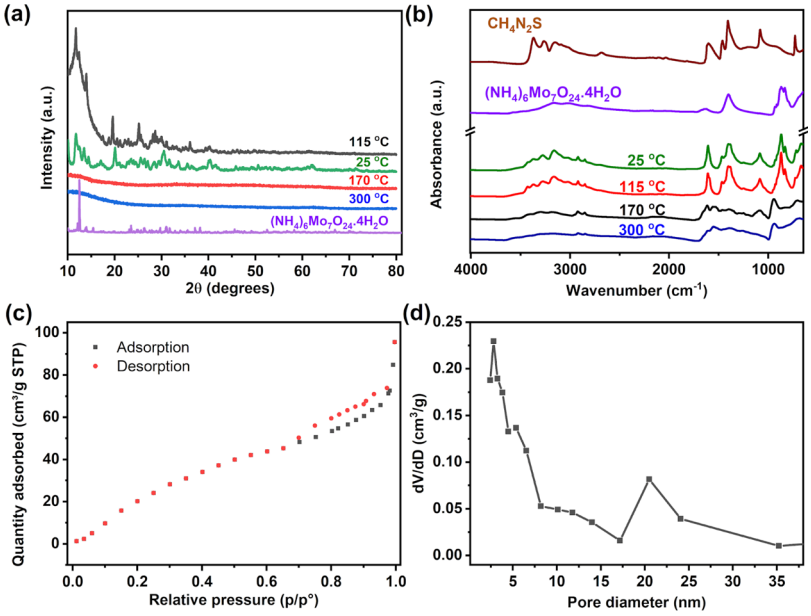


Figure 1. (a) XRD patterns and (b) FTIR spectra of drop-cast LLC mesophases, which were annealed at various temperatures. (c) N_2 adsorption–desorption analysis and (d) pore size distribution of the mesoporous MoS_2.

recorded using XRD was performed using PDF cards of the Bruker EVA software program with the International Center for Diffraction Data (ICDD). Fourier transform infrared (FTIR) spectra of the mesophase and annealed samples were recorded using a PerkinElmer Frontier MIR-ATR spectrometer with a 4 cm^{-1} spectral resolution. A Zeiss Supra 50VP scanning electron microscope (SEM) with an accelerating voltage of 20 kV equipped with an energy-dispersive spectrometer (EDS) was used to analyze the film morphology and composition of the samples. Low- and high- magnification transmission electron microscopy (TEM) images were recorded on a Jeol JEM 2100F field emission electron microscope under 200 kV electron beam energy. Brunauer–Emmett–Teller (BET) surface area analysis and Barrett–Joyner–Halenda (BJH) pore size and volume analysis of all synthesized materials were done using a Micromeritics ASAP 2020 automated gas sorption analyzer. X-ray photoelectron spectroscopy (XPS) measurements were conducted using a Thermo K-alpha spectrometer system with Al Kα radiation (hυ = 1486.7 eV) as the excitation source. Binding energies for the XPS spectra were calibrated by setting C 1s binding energy to 284.5 eV. Raman spectroscopy measurements were carried out using a Renishaw Raman microscope. The power on the sample was about 2 mW/mm^2 with a 532 nm laser.

Electrochemical Measurements. All electrochemical measurements except electrochemical impedance spectroscopy (EIS) were performed using a GAMRY Reference 300 potentiostat/galvanostat in a three-electrode configuration. A graphite rod was used as a counter electrode. The reference electrode was Ag/AgCl (in saturated KCl), and activity measurements were performed in 0.5 M H_2SO_4. The standard potential of a reference electrode was checked relative to another reference electrode that was never used in experiments and was always properly stored. The measured potentials vs Ag/AgCl were converted to the reversible hydrogen electrode (RHE) scale according to the Nernst equation: $E_{RHE} = E_{Ag/AgCl} + 0.059 \times pH + E^{\circ}_{Ag/AgCl}$ ($E^{\circ}_{Ag/AgCl}$ = 0.198 V at 25 °C).

A scan rate of 5 mV/s was used in the linear sweep voltammetry (LSV) measurements. All LSV plots were corrected with %100 IR compensation for ohmic losses. Current interrupt IR compensation mode in the software of GAMRY Reference 3000 potentiostat/galvanostat was selected. In this technique, a current interrupt measurement is done after each point of LSV scans, and a determination of the uncompensated resistance is made based on the drop in the voltage measurement. The electrochemically active surface areas (ECSA) were estimated by taking cyclic voltammetry (CV) scans between 0.14 and 0.26 V vs RHE where capacitive charging/discharging occurred, and no obvious faradic reaction took place. Electrochemical double-layer capacitance (C_{dl}) capacitance was estimated by plotting the anodic and cathodic current density differences $\Delta j = (j_a - j_c)$ at 0.2 V vs RHE as a function of the scan rate. The slopes of these plots were assumed to be twice C_{dl} and used to represent ECSA. The CVs were taken in 0.5 M H_2SO_4 electrolyte solution by increasing scan rates from 50 to 250 mV/s with an interval of 50 mV/s. Charge transfer resistance (R_{ct}) was determined by EIS performed using a Bio-Logic VSP300 potentiostat between 0.01 Hz and 100 kHz at an amplitude of 10 mV without applying any external bias. H_2SO_4 (0.5 M) was used as the electrolyte solution. To determine R_{ct}, Nyquist plots were fitted with an equivalent circuit model created by EC-Lab software.

RESULT AND DISCUSSION

Most transition-metal nitrate salts have a low melting point and high solubility in water that promotes the formation of LLC mesophase with surfactants. However, there is no such Mo precursor available. Ammonium heptamolybdate was rationally selected among Mo precursors because the high pH given by excess ammonia provides extra stability and solubility. However, ammonium heptamolybdate just decomposes at 190 °C before melting.[50] This poses a major problem for the formation of mesophase of ammonium heptamolybdate with surfactants, which is a prerequisite to obtaining mesoporous MoS_2. Therefore, we initially investigated the formation of the LLC mesophase of ammonium heptamolybdate and thiourea and two surfactants, CTAB and polyoxyethylene (10) lauryl ether. The reaction of drop-cast liquid mesophases of ammonium heptamolybdate and thiourea with two surfactants was monitored using XRD and FTIR spectroscopy. The drop-cast layer was annealed for half an hour at various temperatures in an inert N_2 atmosphere.

XRD analysis provides direct information about both the formation and the stability of the LLC mesophase. In the case that mesophase does not form, the precursors and surfactants crystallize after evaporation of the solvent. Many overlapped diffraction lines mostly belonging to ammonium heptamolybdate were observed in the XRD patterns of the samples

Downloaded from pubs.acs.org/aaemcq/article-pdf/5/6/7006/4453682/ae2c00640.pdf by KOC UNIV user on 29 October 2026

https://doi.org/10.1021/acsaem.2c00640
ACS Appl. Energy Mater. 2022, 5, 7006–7015

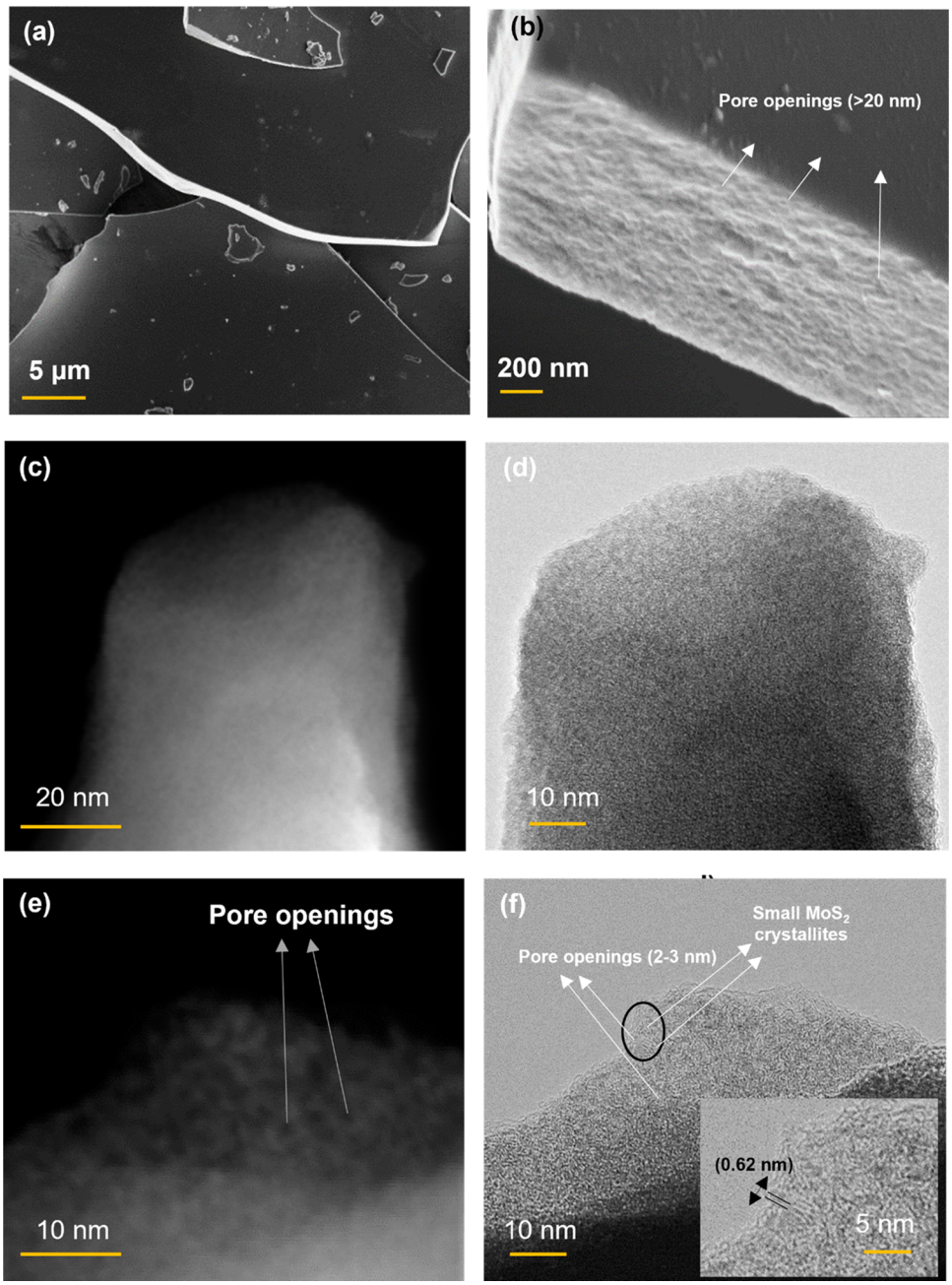


Figure 2. (a, b) SEM images of scratched mesoporous MoS_2 in a different perspective on a copper grid. (c, e) High-angle annular dark-field scanning transmission electron microscopy (HAADF-STEM) and (d, f) low and high magnification TEM images of mesoporous MoS_2, respectively.

annealed at 115 °C (see Figure 1a). On the other hand, the samples annealed at 170 °C and higher temperatures did not reveal any diffraction lines. FTIR spectra of the samples collected at various temperatures were presented with the reference samples of thiourea and ammonium heptamolybdate in Figure 1b. Tracking thiourea peaks in FTIR spectra is critical to detect the complexation of molybdate ions with sulfurous compounds. For thiourea, the peaks at 3383 and 3277 cm^{-1} are assigned to the symmetric and asymmetric stretching vibrations of N−H. The peak at 1620 cm^{-1} corresponds to N−H bending vibration. The absorption observed between 1473 and 1413 cm^{-1} is assigned to the N−C−N symmetric and asymmetric stretching modes. The sharp peak at 729 cm^{-1} is caused by the C−S stretching mode. Spectra obtained from the samples at room temperature and annealed at 115 °C were almost identical. In addition, the fingerprints of thiourea in the samples annealed at 170 °C and higher temperatures were not observed. This indicates that the annealing temperature of 170 °C is adequate for the decomposition of thiourea. The samples at room temperature and 115 °C were opaque while their color turned greenish and dark with increasing annealing temperatures (see Figure S6a). The opacity of the samples correlated with XRD patterns. Crystals of ammonium heptamolybdate salt and thiourea cause opaque color. The sulfurous products from the decomposition of thiourea react with molybdate, resulting in the formation of thiomolybdates (MoS_4^{2-}), giving the samples dark red color. These observations reveal that molybdates cannot form the LLC mesophase. However, the

https://doi.org/10.1021/acsaem.2c00640
ACS Appl. Energy Mater. 2022, 5, 7006−7015

Downloaded from pubs.acs.org/aaemcq/article-pdf/5/6/7006/4453682/ae2c00640.pdf by KOC UNIV user on 29 October 2026

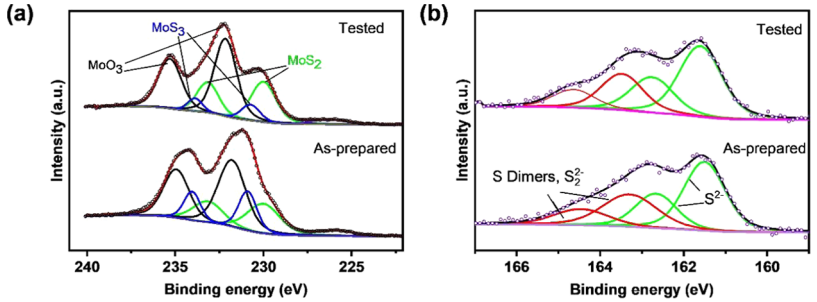


Figure 3. (a) Mo 3d and (b) S 2p XPS spectra of the mesoporous MoS_2 on FTO. The deconvolution of the spectra was performed using the Doniach−Sunjic line profile. A Shirley type of background was used in all spectra. The S 2p spectra were deconvoluted using a doublet with a splitting of 1.2 eV and a 2:1 $2p_{3/2}/2p_{1/2}$ area ratio. The Mo 3d spectra were deconvoluted using a doublet with a splitting of 3.14 eV and a 2:3 $3d_{3/2}/3d_{5/2}$ area ratio.

formed thiomolybdates can be confined among the surfactant domains and form mesophase. This unique behavior is useful for the synthesis of mesoporous MoS_2 thin films.

The spin-coating method enables obtaining thinner and uniform films compared to drop- and dip-coating methods. Water is normally a good choice of solvent owing to its ability to dissolve all precursors and surfactants. However, spin coating accelerates the evaporation of solvents in the liquid templating methods. Ethylene glycol, usually named organic water, has a higher boiling point (197 °C) and has almost the same ability to dissolve hydrophilic compounds or ionic species. The addition of ethylene glycol into a typical solution of CTAB, $C_{12}EO_{10}$, ammonium heptamolybdate, and thiourea can provide the exposure time required during spin coating. Because the viscosity of ethylene glycol is higher than that of deionized water, its amount was kept limited to get even overlayers without pits and holes.

As demonstrated in Figure S6b, the color of the transparent samples, which were prepared by spin coating of typical solution with ethylene glycol, turned to homogenous yellowish-green after annealing at 115 °C. Further annealing at higher temperatures changed them to yellow and then dark brown. Similar color changes were observed as the annealing temperatures of drop-cast films were raised. Besides, the crystallization of ammonium molybdate salts caused by leaching out of the mesophase was not observed as evidenced by the absence of the XRD patterns of the spin-coated samples at room temperature and further annealed at 115 °C (see Figure S7). The deionized water evaporates during spinning, and the remaining ethylene glycol keeps dissolving all ingredients required for the LLC mesophase integrity. Rapid direct annealing of spin-coated samples at 170 °C evaporates the remaining ethylene glycol. Meanwhile, thiourea directly decomposes into sulfurous products at those temperatures (it decomposes at around 130 °C), producing thiomolybdates. The changes in the diffraction lines at small-angle XRD of the as-prepared and annealed samples presented in Figure S7a suggest that the addition of ethylene glycol to the solution prevents the crystallization of ingredients and enables the formation of LLC mesophase required for the synthesis of mesoporous MoS_2 thin films. The addition of ethylene glycol does not alter XRD patterns and thus mesoporous samples of similar crystallinity form (see Figure S7b). As in the protocol for the preparation of mesoporous nickel sulfides, capping during annealing cannot be applied to prevent the escape of sulfurous gases from the mesophase without reacting molybdate ions. When we apply the sandwich structure after spin coating, the sol between two substrates shrinks and aggregates randomly on the surface of the substrates during evaporation of ethylene glycol at 170 °C. This hinders the formation of thin films.

To prove that fast annealing of the LLC mesophase of ammonium heptamolybdate salt, thiourea, and two surfactants produces mesoporous MoS_2, the N_2 adsorption−desorption isotherm of the sample annealed at 300 °C was recorded (Figure 1c). The hysteresis on the adsorption and desorption behavior confirms the mesoporosity. The BET surface area is about 182 m^2/g. The BJH analysis exhibits a narrow pore-size distribution peaking around 3 nm and a broad pore-size distribution starting above 30 nm (Figure 1d). The mesopore size (∼3 nm) is consistent with the size of surfactant domains in the LLC mesophase. The pore size distribution greater than the expected micelle sizes (2−3 nm) may be originating from the harsh release of decomposed gaseous compounds induced by annealing.

To identify the structural form of the surfactant after annealing, Raman analysis of the mesoporous MoS_2 was performed, and the resulting spectrum is presented in Figure S8. In carbon, the Stokes phonon energy shift caused by laser excitation creates two main peaks in the Raman spectrum: graphitic peak G (1580 cm^{-1}), a primary in-plane vibrational mode, and an out-of-plane vibration, defect peak D (1350 cm^{-1}). The Raman spectrum is considered to mainly depend on the sp^2/sp^3 ratio. The intensity ratio of D to G peaks is below 1, suggesting an amorphous structure. Surfactants in the mesophase structure were carbonized by annealing; mesopores were not clogged by amorphous carbon. They could be suspended in the mesoporous framework due to the volumetric shrinkage during decomposition. Such a process provides an extra surface area on the sample. The BET surface area, 182 m^2/g, does not belong solely to MoS_2 nanocrystallites.

SEM images of scratched mesoporous MoS_2 thin-film samples presented in Figure 2a,b show nontextured surface features. On the other hand, the interior of the films has pores of 20−25 nm in size, which is consistent with the pore size distribution derived from the N_2 sorption analysis. The sizes of smaller mesopores are under the resolving limit of SEM. EDS of the sample performed for the compositional analysis indicates that the Mo/S atomic ratio of the sample is about 1:1, smaller than the expected ratio, 1:2 (Figure S9). This could indicate that a large fraction of Mo is still in its oxide form even though the Mo/S precursor ratio was adjusted to be 1:2.

Downloaded from pubs.acs.org/aaemcq/article-pdf/5/6/7006/4453682/ae2c00640.pdf by KOC UNIV user on 29 October 2026

https://doi.org/10.1021/acsaem.2c00640
ACS Appl. Energy Mater. 2022, 5, 7006−7015

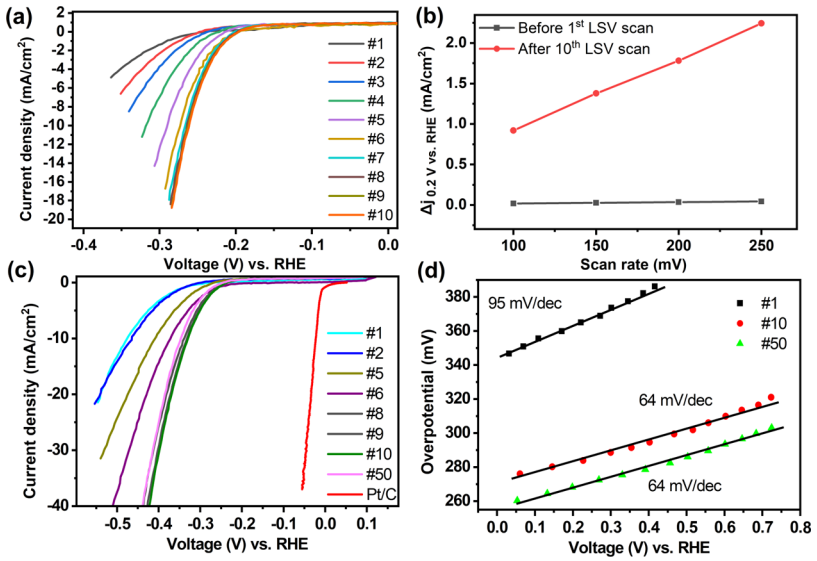


Figure 4. (a) Consecutive LSV plots in 0.5 M H_2SO_4 for mesoporous MoS_2 and the commercial Pt/C on FTO prepared at 300 °C. (b) Capacitive currents plots as a function of the scan rate before the 1st LSV scan and after the 10th LSV scan. The plots were derived from CV scans in Figure S12. (c) Long-term stability test in 0.5 M H_2SO_4. Consecutive LSV plots for mesoporous MoS_2 on FTO prepared at 300 °C. (d) Tafel plots of mesoporous MoS_2 on FTO prepared at 300 °C for various consecutive LSV plots.

To further understand the structural details of the mesoporous MoS_2 films, TEM images have also been recorded. High-angle annular dark-field (HAADF) STEM images, in Figure 2c,e, and TEM images, in Figure 2d,f, display the sponge-like disordered mesoporosity with 3−5 nm wide pore openings. In the selected microscopic area of the sample, the sizes of the pore openings are consistent with the sizes of the micelles formed by CTAB and $C_{12}EO_{10}$ (see Figure S10). In the high-resolution TEM images (Figure 2f), the lattice fringes of MoS_2 nanocrystals (0.62 nm representing (200) lattice planes) can be observed.

XPS measurements were performed to further identify the surface compositions of the electrodes. The results of the XPS analysis of as-prepared mesoporous MoS_2 are shown in Figure 3a,b. Reported XPS studies of the MoS_2 formation from ammonium tetrathiomolybdate solutions are useful for the assignment of Mo 3d and S 2p peaks[51] In Figure 3a, the Mo 3d double peaks at 232.3 and 229.1 eV are assigned to Mo^{4+} in MoS_2. Moreover, two sets of double peaks at 231.45 and 230.95 eV and at 235.6 and 232.2 eV were observed, which originate from the MoS_3 and MoO_3 formed by unconverted molybdate ions, respectively. For the S 2p XPS spectra presented in Figure 3b, the doublet peaks at 161.3/162.5 eV are ascribed to the S_2^{2-}, while the major doublets at 163.8/165.0 eV were attributed to S^{2-} dimers, originating from amorphous MoS_3 and MoS_2 edges. Combining XRD, TEM, STEM, EDS, and XPS results, we can reveal that mesoporous MoS_2 thin films consist of a mixture of nanocrystalline MoS_2, amorphous MoS_3, and amorphous MoO_3 with mesoporous structure.

We investigated the HER activities of mesoporous MoS_2 thin-film electrodes on the FTO in an acidic electrolyte, 0.5 M H_2SO_4. Ten consecutive LSV scans were recorded for each electrode, and the progress of the LSV curves is demonstrated in Figure 4a. It was observed that the HER activity of the sample annealed at 300 °C was dynamic, and each LSV scan showed better activity in terms of lower onset potential and higher current density than the previous one. After the sixth scan, no further change in the LSV curves was observed. Ten consecutive LSV scans were also recorded for electrodes prepared at 400 and 500 °C to check the effect of annealing temperature on the HER activity (see Figure S11). The most active sample toward the HER in an acidic environment was the one annealed at 300 °C. Higher annealing temperatures reduced the HER activity dramatically. HER activities for these samples showed no improvement with LSV scans as observed in the sample annealed at 300 °C. It was observed that consecutive LSV scans did not exhibit any significant change.

ECSAs of the electrodes are typically proportional to the electric double-layer capacitance (C_{dl}), which can be derived from the CV curves in a nonfaradic region. Therefore, we tracked the changes in the CV curves of mesoporous MoS_2 after the stabilization performed by successive LSV scans (Figure S12). It was observed by comparing capacitive current plots before the 1st and after the 10th LSV scan as a function of the scan rate that the ECSA of the tested sample annealed at 300 °C increased at least 5 times (Figure 4b). Other samples showed the same trend to a lesser extent. The calculated ECSA of tested samples annealed at 400 and 500 °C are around 4 times less than the tested sample annealed at 300 °C. We stressed that samples annealed at 400 and 500 °C did not show any porosity in N_2 sorption measurements. As expected, this explains the limited HER performance of these samples. The increase in ECSA represented the correlation with the enhancement in HER activity. Apparently, there is an electrochemical activation process during the HER.

To ascertain the long-term changes in HER activity, consecutive LSV curves under high potentials and current densities were recorded (Figure 4c). Even under high current densities, the HER activity was maximized at the 10th cycle and then slightly decreased. The HER started with an overpotential of 476 mV and reduced to 332 mV at the current density of 10 mA/cm^2. It was presumed that intensified evolution of H_2 bubbles on the film structure might delaminate film structure. The Tafel plots in Figure 4d showed that the first LSV cycle possesses the highest Tafel slope, 95 mV/dec, in

Downloaded from pubs.acs.org/aaemcq/article-pdf/5/6/7006/4453682/ae2c00640.pdf by KOC UNIV user on 29 October 2026

https://doi.org/10.1021/acsaem.2c00640
ACS Appl. Energy Mater. 2022, 5, 7006−7015

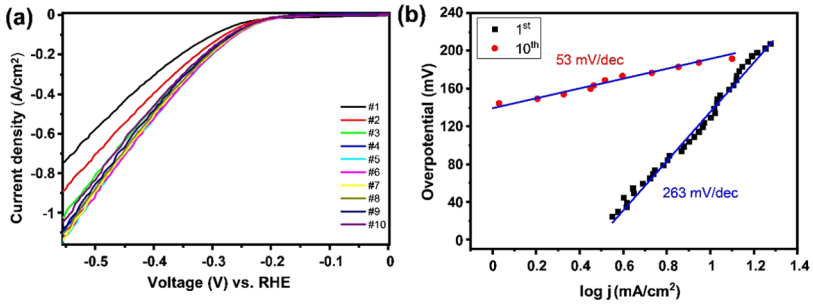


Figure 5. (a) Consecutive LSV plots and (b) Tafel plots for mesoporous MoS_2 on carbon fiber prepared at 300 °C, in 0.5 M H_2SO_4.

comparison to 64 mV/dec obtained after the 10th and 50th LSV scans, demonstrating the superior HER kinetics. Delamination of the catalyst over extensive HER was a much plausible explanation since the Tafel slopes did not vary. The loss of electrocatalyst decreases only the current density and does not affect the HER kinetics. The amendment in the kinetics of HER might be related to the changes in the active sites. If the number of active species with the same characteristics is increased during HER by reasons like the dissolution of surface species blocking active HER sites, ESCA could increase but Tafel slopes do not necessarily change. Therefore, we assume that the synthesized mesoporous MoS_2 sample shows precatalyst property that transforms into a much superior electrocatalyst for the HER.

To further apprehend the structural changes and the HER activity enhancement during the HER, we performed XPS measurements on an LSV-tested sample. The results of the XPS analysis given in Figure 3a,b indicated that the intensity of double peaks at 231.4 and 231.6 eV in the Mo 3d spectrum, which originated from the MoS_3, decreased compared to the as-prepared sample. The intensity of MoS_2 species significantly increased, while those of the MoO_3 species remained largely unchanged. The relative ratio of S 2p doublet peaks at 161.3/162.5 eV and 163.8/165.0 eV slightly increased compared to the as-prepared sample. Sulfur dimers originating from MoS_3 could be converted to ultrasmall nanocrystalline MoS_2 species because of having a high number of sulfur dimers at the edges. It was revealed that most of the amorphous MoS_3 species in the mesoporous framework are reduced to superior active species, MoS_2. It is also observed in the literature that amorphous MoS_3 undergoes in situ self-reconstruction and the formation of MoS_2 species during the HER.[9,10] The SEM/EDS analysis also was performed for tracking the composition and morphology of LSV-tested electrocatalyst films on FTO (see Figure S13a,b). The Mo/S atomic ratio was increased, but there were no significant changes in the morphology. This electrochemical activation is limited by the surface of the mesoporous framework. We observed that MoS_3 species cannot be electrochemically converted to MoS_2 as a whole because of the lack of contact with the electrolyte. We can presume that MoS_2 nanodomains were embedded in the amorphous MoO_3 and MoS_3 matrix of the mesoporous framework. Amorphous MoO_3 species do not present a pronounced HER activity.[52] This activity enhancement owing to the transformation of MoS_3 to MoS_2 in the surface regime is also associated with the reduced charge transfer resistance (R_{ct}) determined by the analysis of Nyquist plots (see Figure S14).

Carbon-based materials are generally used as a support material for hydrogen electrodes to increase the overall conductivity and surface area of the electrocatalyst. Ten consecutive LSV scans of mesoporous MoS_2 on carbon fiber within a cathodic potential window in the range of 0 to −0.6 V vs RHE were recorded (Figure 5a), and the Tafel plots of the 1st and final LSVs were calculated (Figure 5b). Similar to the mesoporous samples on FTO, each LSV curve exhibited better activity than the previous one. It can be seen that the 10th LSV cycle showed the lowest onset overpotential of ∼189 mV at 10 mA/cm^2 for the HER, beyond which the cathodic current density rises rapidly under more negative potentials. Commercial electrolyzers should operate at large current densities around 1−2 A/cm^2. The electrode on carbon fiber can reach 1 A/cm^2 with the overpotential of ∼550 mV owing to the highly porous character of the electrodes. As expected, the sample on carbon fiber displayed faster HER kinetics than the sample on FTO since the Tafel slope of the sample on carbon fiber (53 mV/dec) was lower than that of the sample on FTO (64 mV/dec). As shown in Table S3, the values of Tafel slopes and the overpotentials at various current densities are comparable with most of the reported MoS_2-based HER electrocatalysts. In acidic media, Volmer−Heyrovsky ($H^+ + e^- \rightarrow H_{ad}$, $H^+ + H_{ad} + e^- \rightarrow H_2$) and Volmer−Tafel ($H^+ + e^- \rightarrow H_{ad}$, $H_{ad} + H_{ad} \rightarrow H_2$) processes are plausible.[53] The theoretical Tafel slope values for the Volmer reaction, Heyrovsky reaction, and Tafel reaction are 118, 39, and 29.5 mV/dec, respectively.[54] From these findings, we can suggest that the HER follows the Volmer−Heyrovsky mechanism initially when MoS_3 as a precatalyst is a dominant phase. With electrochemical activation, the reduction of MoS_3 into MoS_2 nanodomains, the mechanism likely advances toward Volmer−Tafel. MoS_2 nanodomains are likely to have abundant edge sites. The overpotential at 10 mA/cm^2 and Tafel slopes of some recently reported MoS_2-based electrocatalysts are listed in Table S3. Bare MoS_2 electrocatalysts show a similar range of overpotentials at 10 mA/cm^2, around 200 mV, and a comparison with its analogues revealed that the mesoporous MoS_2 demonstrated quite outstanding performance in terms of its overpotential and Tafel slope.[21,27,43,55,56] Doping with high valance atoms (W, Nb, Mo, etc.) and supporting with a substrate of a superior conductive high surface area, such as carbon nanotube foam or graphene foam, our mesoporous electrodes may provide much more active sites and internal conductivity, leading to Pt-like activity.[28] TOF at 300 mV overpotential was estimated to be 2.7 s^{-1}, which is comparable with those from MoS_2 prepared by conventional methods.[57] We can suggest that our novel soft templating method could be a promising coating technology to prepare low-cost and highly efficient MoS_2 HER binder-free electrodes on any support materials. To show the applicability of our synthesis protocol to the commercial roll-to-roll coating technology for

Downloaded from pubs.acs.org/aaemcq/article-pdf/5/6/7006/4453682/ae2c00640.pdf by KOC UNIV user on 29 October 2026

https://doi.org/10.1021/acsaem.2c00640
ACS Appl. Energy Mater. 2022, 5, 7006−7015

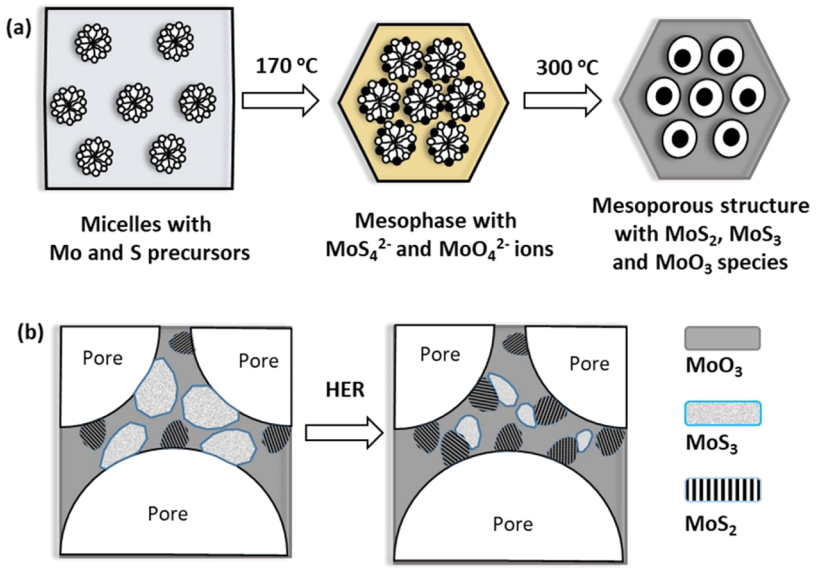


Figure 6. (a) Schematic diagram of the liquid templating method for mesoporous MoS_2 and (b) in situ structural transformation during the HER.

membrane-electrode-assemblies (MEA), we applied mesoporous MoS_2−MoO_3 composite electrocatalyst on a commercial carbon cloth with a microporous layer electrode. The mesoporous MoS_2−MoO_3 on this electrode showed outstanding stability over 20 h at a constant overpotential of 300 mV (see Figure S15). H_2 bubbles were not formed on the MoS_2−MoO_3 coated microporous layer side of the electrode during the HER, and H_2 gas easily vent off from carbon cloth (Video S1).

CONCLUSIONS

Active, durable, and abundant non-platinum group material (PGM)-based electrocatalysts are crucial for green hydrogen production. MoS_2 has been one of the best candidates and the most studied non-PGM electrocatalyst. Mesoporous thin-film materials also provide an ideal platform for improved charge transfer kinetics and reagent/product diffusion provided by their high surface area and integrated continuous nanostructure for the HER. We showed, for the first time, a novel protocol to produce mesoporous thin-film MoS_2 synthesized by a novel soft templating method without postsulfurization, as represented in Figure 6a. The present results suggest that a mesoporous framework has a narrow pore size distribution form and consists of embedded MoS_2 nanocrystals within the continuous amorphous MoS_3 and MoO_3 moieties, as demonstrated in Figure 6b. The samples exhibited superior HER activity in an acidic media after a structural transformation from MoS_3 to MoS_2 via an electrochemical reduction during the HER. In situ electrochemical activation boosts the ECSA and reduces the Tafel slopes, leading to lower overpotential and better kinetics for the HER. This outcome increased durable sulfur-terminated edges on MoS_2 as HER active sites.

ASSOCIATED CONTENT

Supporting Information

The Supporting Information is available free of charge at https://pubs.acs.org/doi/10.1021/acsaem.2c00640.

Schematic representation of the synthesis protocols, XRD patterns of the samples annealed at various temperatures, SEM images, line profiles from the HAADF-STEM images, annealing temperature effects on LSV scans, CV curves for ECSA determination, Nyquist plots, CA measurement, and TOF estimation (PDF)

AUTHOR INFORMATION

Corresponding Author

Sarp Kaya − *Materials Science and Engineering, Koç University, 34450 Istanbul, Turkey; Koç University Tüpraş Energy Center (KUTEM), 34450 Istanbul, Turkey; Department of Chemistry, Koç University, 34450 Istanbul, Turkey;* orcid.org/0000-0002-2591-5843; Email: sarpkaya@ku.edu.tr

Authors

Cüneyt Karakaya − *Materials Science and Engineering, Koç University, 34450 Istanbul, Turkey; Koç University Tüpraş Energy Center (KUTEM), 34450 Istanbul, Turkey; Tüpraş R&D, 41790 Kocaeli, Turkey*

Navid Solati − *Materials Science and Engineering, Koç University, 34450 Istanbul, Turkey; Koç University Tüpraş Energy Center (KUTEM), 34450 Istanbul, Turkey*

Timuçin Balkan − *Koç University Tüpraş Energy Center (KUTEM), 34450 Istanbul, Turkey; Department of Chemistry, Koç University, 34450 Istanbul, Turkey*

Umut Savacı − *Department of Materials Science and Engineering, Eskişehir Technical University (ESTU), 26555 Eskişehir, Turkey;* orcid.org/0000-0002-5801-9666

Emre Keleş − *Department of Materials Science and Engineering, Eskişehir Technical University (ESTU), 26555 Eskişehir, Turkey*

Servet Turan − *Department of Materials Science and Engineering, Eskişehir Technical University (ESTU), 26555 Eskişehir, Turkey;* orcid.org/0000-0002-7322-3091

Complete contact information is available at: https://pubs.acs.org/10.1021/acsaem.2c00640

Notes

The authors declare no competing financial interest.

Downloaded from pubs.acs.org/aaemcq/article-pdf/5/6/7006/4453682/ae2c00640.pdf by KOC UNIV user on 29 October 2026

https://doi.org/10.1021/acsaem.2c00640
ACS Appl. Energy Mater. 2022, 5, 7006−7015

■ ACKNOWLEDGMENTS

The authors thank Koç University Surface Science and Technology Center (KUYTAM) for providing Raman spectroscopy and XPS analysis. C.K. thanks technicians of Tüpraş R&D Center Laboratories for collaborative research support.

■ REFERENCES

(1) *Reaching Zero with Renewables: Eliminating CO2 Emissions from Industry and Transport in Line with the 1.5 ^{O}C Climate Goal*; International Renewable Energy Agency (IRENA): Abu Dhabi, 2020.
(2) *Green Hydrogen Cost Reduction: Scaling up Electrolysers to Meet the 1.5 °C Climate Goal*; International Renewable Energy Agency (IRENA): Abu Dhabi, 2020.
(3) Cheng, N.; Stambula, S.; Wang, D.; Banis, M. N.; Liu, J.; Riese, A.; Xiao, B.; Li, R.; Sham, T.-K.; Liu, L.-M.; Botton, G. A.; Sun, X. Platinum Single-Atom and Cluster Catalysis of the Hydrogen Evolution Reaction. *Nat. Commun.* **2016**, *7*, No. 13638.
(4) Roukoss, C.; Laurenti, D.; Devers, E.; Marchand, K.; Massin, L.; Vrinat, M. Hydrodesulfurization Catalysts: Promoters, Promoting Methods and Support Effect on Catalytic Activities. *C. R. Chim.* **2009**, *12*, 683−691.
(5) Hinnemann, B.; Moses, P. G.; Bonde, J.; Jørgensen, K. P.; Nielsen, J. H.; Horch, S.; Chorkendorff, I.; Nørskov, J. K. Biomimetic Hydrogen Evolution: MoS_2 Nanoparticles as Catalyst for Hydrogen Evolution. *J. Am. Chem. Soc.* **2005**, *127*, 5308−5309.
(6) Jaramillo, T. F.; Jørgensen, K. P.; Bonde, J.; Nielsen, J. H.; Horch, S.; Chorkendorff, I. Identification of Active Edge Sites for Electrochemical H2 Evolution from MoS_2 Nanocatalysts. *Science* **2007**, *317*, 100−102.
(7) Li, G.; Zhang, D.; Qiao, Q.; Yu, Y.; Peterson, D.; Zafar, A.; Kumar, R.; Curtarolo, S.; Hunte, F.; Shannon, S.; Zhu, Y.; Yang, W.; Cao, L. All The Catalytic Active Sites of MoS_2 for Hydrogen Evolution. *J. Am. Chem. Soc.* **2016**, *138*, 16632−16638.
(8) Lv, C.; Yan, C.; Chen, G.; Ding, Y.; Sun, J.; Zhou, Y.; Yu, G. An Amorphous Noble-Metal-Free Electrocatalyst That Enables Nitrogen Fixation under Ambient Conditions. *Angew. Chem.* **2018**, *130*, 6181−6184.
(9) Merki, D.; Fierro, S.; Vrubel, H.; Hu, X. Amorphous Molybdenum Sulfide Films as Catalysts for Electrochemical Hydrogen Production in Water. *Chem. Sci.* **2011**, *2*, 1262−1267.
(10) Casalongue, H. G. S.; Benck, J. D.; Tsai, C.; Karlsson, R. K. B.; Kaya, S.; Ng, M. L.; Pettersson, L. G. M.; Abild-Pedersen, F.; Nørskov, J. K.; Ogasawara, H.; Jaramillo, T. F.; Nilsson, A. Operando Characterization of an Amorphous Molybdenum Sulfide Nanoparticle Catalyst during the Hydrogen Evolution Reaction. *J. Phys. Chem. C* **2014**, *118*, 29252−29259.
(11) Lee, S. C.; Benck, J. D.; Tsai, C.; Park, J.; Koh, A. L.; Abild-Pedersen, F.; Jaramillo, T. F.; Sinclair, R. Chemical and Phase Evolution of Amorphous Molybdenum Sulfide Catalysts for Electrochemical Hydrogen Production. *ACS Nano* **2016**, *10*, 624−632.
(12) Yu, Y.; Huang, S.-Y.; Li, Y.; Steinmann, S. N.; Yang, W.; Cao, L. Layer-Dependent Electrocatalysis of MoS_2 for Hydrogen Evolution. *Nano Lett.* **2014**, *14*, 553−558.
(13) Lv, Z.; Mahmood, N.; Tahir, M.; Pan, L.; Zhang, X.; Zou, J.-J. Fabrication of Zero to Three Dimensional Nanostructured Molybdenum Sulfides and Their Electrochemical and Photocatalytic Applications. *Nanoscale* **2016**, *8*, 18250−18269.
(14) Ding, J.; Zhou, Y.; Li, Y.; Guo, S.; Huang, X. MoS_2 Nanosheet Assembling Superstructure with a Three-Dimensional Ion Accessible Site: A New Class of Bifunctional Materials for Batteries and Electrocatalysis. *Chem. Mater.* **2016**, *28*, 2074−2080.
(15) Ren, X.; Pang, L.; Zhang, Y.; Ren, X.; Fan, H.; Liu, S. Frank. One-Step Hydrothermal Synthesis of Monolayer MoS_2 Quantum Dots for Highly Efficient Electrocatalytic Hydrogen Evolution. *J. Mater. Chem. A* **2015**, *3*, 10693−10697.
(16) Guo, B.; Yu, K.; Li, H.; Song, H.; Zhang, Y.; Lei, X.; Fu, H.; Tan, Y.; Zhu, Z. Hollow Structured Micro/Nano MoS_2 Spheres for High Electrocatalytic Activity Hydrogen Evolution Reaction. *ACS Appl. Mater. Interfaces* **2016**, *8*, 5517−5525.
(17) Ren, X.; Wei, Q.; Ren, P.; Wang, Y.; Chen, R. Synthesis of Flower-like $MoSe_2$@MoS_2 Nanocomposites as the High Efficient Water Splitting Electrocatalyst. *Mater. Lett.* **2018**, *231*, 213−216.
(18) Yan, Y.; Xia, B.; Ge, X.; Liu, Z.; Wang, J.-Y.; Wang, X. Ultrathin MoS_2 Nanoplates with Rich Active Sites as Highly Efficient Catalyst for Hydrogen Evolution. *ACS Appl. Mater. Interfaces* **2013**, *5*, 12794−12798.
(19) Cao, Y. Roadmap and Direction toward High-Performance MoS2 Hydrogen Evolution Catalysts. *ACS Nano* **2021**, *15*, 11014−11039.
(20) Zhu, H.; Du, M.; Zhang, M.; Zou, M.; Yang, T.; Wang, S.; Yao, J.; Guo, B. S-Rich Single-Layered MoS_2 Nanoplates Embedded in N-Doped Carbon Nanofibers: Efficient Co-Electrocatalysts for the Hydrogen Evolution Reaction. *Chem. Commun.* **2014**, *50*, 15435−15438.
(21) Guo, Y.; Zhang, X.; Zhang, X.; You, T. Defect- and S-Rich Ultrathin MoS_2 Nanosheet Embedded N-Doped Carbon Nanofibers for Efficient Hydrogen Evolution. *J. Mater. Chem. A* **2015**, *3*, 15927−15934.
(22) Yan, Y.; Xia, B.; Li, N.; Xu, Z.; Fisher, A.; Wang, X. Vertically Oriented MoS_2 and WS_2 Nanosheets Directly Grown on Carbon Cloth as Efficient and Stable 3-Dimensional Hydrogen-Evolving Cathodes. *J. Mater. Chem. A* **2015**, *3*, 131−135.
(23) Zhang, N.; Gan, S.; Wu, T.; Ma, W.; Han, D.; Niu, L. Growth Control of MoS_2 Nanosheets on Carbon Cloth for Maximum Active Edges Exposed: An Excellent Hydrogen Evolution 3D Cathode. *ACS Appl. Mater. Interfaces* **2015**, *7*, 12193−12202.
(24) Han, X.; Wu, X.; Deng, Y.; Liu, J.; Lu, J.; Zhong, C.; Hu, W. Ultrafine Pt Nanoparticle-Decorated Pyrite-Type CoS_2 Nanosheet Arrays Coated on Carbon Cloth as a Bifunctional Electrode for Overall Water Splitting. *Adv. Energy Mater.* **2018**, *8*, No. 1800935.
(25) Choi, Y.-H.; Lee, J.; Parija, A.; Cho, J.; Verkhoturov, S. V.; Al-Hashimi, M.; Fang, L.; Banerjee, S. An in Situ Sulfidation Approach for the Integration of MoS_2 Nanosheets on Carbon Fiber Paper and the Modulation of Its Electrocatalytic Activity by Interfacing with NC60. *ACS Catal.* **2016**, *6*, 6246−6254.
(26) Huang, H.; Huang, W.; Yang, Z.; Huang, J.; Lin, J.; Liu, W.; Liu, Y. Strongly Coupled MoS_2 Nanoflake−Carbon Nanotube Nanocomposite as an Excellent Electrocatalyst for Hydrogen Evolution Reaction. *J. Mater. Chem. A* **2017**, *5*, 1558−1566.
(27) Liao, L.; Zhu, J.; Bian, X.; Zhu, L.; Scanlon, M. D.; Girault, H. H.; Liu, B. MoS_2 Formed on Mesoporous Graphene as a Highly Active Catalyst for Hydrogen Evolution. *Adv. Funct. Mater.* **2013**, *23*, 5326−5333.
(28) Li, C.; Zhao, S.; Zhu, K.; Wang, B.; Wang, E.; Luo, Y.; He, L.; Wang, J.; Jiang, K.; Fan, S.; Li, J.; Liu, K. Flexible and Free-Standing Hetero-Electrocatalyst of High-Valence-Cation Doped MoS_2/MoO_2/CNT Foam with Synergistically Enhanced Hydrogen Evolution Reaction Catalytic Activity. *J. Mater. Chem. A* **2020**, *8*, 14944−14954.
(29) Ye, G.; Gong, Y.; Lin, J.; Li, B.; He, Y.; Pantelides, S. T.; Zhou, W.; Vajtai, R.; Ajayan, P. M. Defects Engineered Monolayer MoS_2 for Improved Hydrogen Evolution Reaction. *Nano Lett.* **2016**, *16*, 1097−1103.
(30) Kang, S.; Koo, J.-J.; Seo, H.; Truong, Q. T.; Park, J. B.; Park, S. C.; Jung, Y.; Cho, S.-P.; Nam, K. T.; Kim, Z. H.; Hong, B. H. Defect-Engineered MoS_2 with Extended Photoluminescence Lifetime for High-Performance Hydrogen Evolution. *J. Mater. Chem. C* **2019**, *7*, 10173−10178.
(31) Kim, Y.; Jackson, D. H. K.; Lee, D.; Choi, M.; Kim, T.-W.; Jeong, S.-Y.; Chae, H.-J.; Kim, H. W.; Park, N.; Chang, H.; Kuech, T. F.; Kim, H. J. In Situ Electrochemical Activation of Atomic Layer Deposition Coated MoS_2 Basal Planes for Efficient Hydrogen Evolution Reaction. *Adv. Funct. Mater.* **2017**, *27*, No. 1701825.
(32) Tsai, C.; Li, H.; Park, S.; Park, J.; Han, H. S.; Nørskov, J. K.; Zheng, X.; Abild-Pedersen, F. Electrochemical Generation of Sulfur Vacancies in the Basal Plane of MoS_2 for Hydrogen Evolution. *Nat. Commun.* **2017**, *8*, No. 15113.

Downloaded from pubs.acs.org/aaemcq/article-pdf/5/6/7006/4453682/ae2c00640.pdf by KOC UNIV user on 29 October 2026

https://doi.org/10.1021/acsaem.2c00640
ACS Appl. Energy Mater. 2022, 5, 7006−7015

(33) Xu, X.; Liu, W.; Kim, Y.; Cho, J. Nanostructured Transition Metal Sulfides for Lithium Ion Batteries: Progress and Challenges. *Nano Today* **2014**, *9*, 604−630.
(34) Miao, R.; Dutta, B.; Sahoo, S.; He, J.; Zhong, W.; Cetegen, S. A.; Jiang, T.; Alpay, S. P.; Suib, S. L. Mesoporous Iron Sulfide for Highly Efficient Electrocatalytic Hydrogen Evolution. *J. Am. Chem. Soc.* **2017**, *139*, 13604−13607.
(35) Rodríguez-Castellón, E.; Jiménez-López, A.; Eliche-Quesada, D. Nickel and Cobalt Promoted Tungsten and Molybdenum Sulfide Mesoporous Catalysts for Hydrodesulfurization. *Fuel* **2008**, *87*, 1195−1206.
(36) Yang, H.; Wang, B.; Li, H.; Ni, B.; Wang, K.; Zhang, Q.; Wang, X. Trimetallic Sulfide Mesoporous Nanospheres as Superior Electrocatalysts for Rechargeable Zn−Air Batteries. *Adv. Energy Mater.* **2018**, *8*, No. 1801839.
(37) Ding, J.; Hong, B.; Luo, Z.; Sun, S.; Bao, J.; Gao, C. Mesoporous Monoclinic $CaIn_2S_4$ with Surface Nanostructure: An Efficient Photocatalyst for Hydrogen Production under Visible Light. *J. Phys. Chem. C* **2014**, *118*, 27690−27697.
(38) Yaman, M. Y.; Han, A. S.; Bandara, J.; Karakaya, C.; Dag, Ö. Modifying Titania Using the Molten-Salt-Assisted Self-Assembly Process for Cadmium Selenide−Quantum Dot-Sensitized Photoanodes. *ACS Omega* **2017**, *2*, 4982−4990.
(39) Türker, Y.; Karakaya, C.; Dag, Ö. Fabrication of Mesoporous Metal Chalcogenide Nanoflake Silica Thin Films and Spongy Mesoporous CdS and CdSe. *Chem. - Eur. J.* **2012**, *18*, 3695−3705.
(40) Karakaya, C.; Türker, Y.; Albayrak, C.; Dag, Ö. Assembly of Molten Transition Metal Salt−Surfactant in a Confined Space for the Synthesis of Mesoporous Metal Oxide-Rich Metal Oxide−Silica Thin Films. *Chem. Mater.* **2011**, *23*, 3062−3071.
(41) Yonemoto, B. T.; Hutchings, G. S.; Jiao, F. A General Synthetic Approach for Ordered Mesoporous Metal Sulfides. *J. Am. Chem. Soc.* **2014**, *136*, 8895−8898.
(42) Shi, Y.; Wan, Y.; Liu, R.; Tu, B.; Zhao, D. Synthesis of Highly Ordered Mesoporous Crystalline WS_2 and MoS_2 via a High-Temperature Reductive Sulfuration Route. *J. Am. Chem. Soc.* **2007**, *129*, 9522−9531.
(43) Kibsgaard, J.; Chen, Z.; Reinecke, B. N.; Jaramillo, T. F. Engineering the Surface Structure of MoS_2 to Preferentially Expose Active Edge Sites for Electrocatalysis. *Nat. Mater.* **2012**, *11*, 963−969.
(44) Guo, Y.; Tang, J.; Henzie, J.; Jiang, B.; Xia, W.; Chen, T.; Bando, Y.; Kang, Y.-M.; Hossain, M. S. A.; Sugahara, Y.; Yamauchi, Y. Mesoporous Iron-Doped $MoS_2/CoMo_2S_4$ Heterostructures through Organic−Metal Cooperative Interactions on Spherical Micelles for Electrochemical Water Splitting. *ACS Nano* **2020**, *14*, 4141−4152.
(45) Amirzhanova, A.; Karakaya, I.; Berk Uzundal, C.; Karaoğlu, G.; Karadas, F.; Ülgüt, B.; Dag, Ö. Synthesis and Water Oxidation Electrocatalytic and Electrochromic Behaviours of Mesoporous Nickel Oxide Thin Film Electrodes. *J. Mater. Chem. A* **2019**, *7*, 22012−22020.
(46) Amirzhanova, A.; Akmanşen, N.; Karakaya, I.; Dag, Ö. Mesoporous $MnCo_2O_4$, $NiCo_2O_4$, and $ZnCo_2O_4$ Thin-Film Electrodes as Electrocatalysts for the Oxygen Evolution Reaction in Alkaline Solutions. *ACS Appl. Energy Mater.* **2021**, *4*, 2769−2785.
(47) Karakaya, I.; Karadas, F.; Ulgut, B.; Dag, Ö. Modification of Mesoporous $LiMn_2O_4$ and $LiMn_2-xCo_xO_4$ by SILAR Method for Highly Efficient Water Oxidation Electrocatalysis. *Adv. Mater. Technol.* **2020**, *5*, No. 2000353.
(48) Balci, F. M.; Karakaya, I.; Pınar Alsaç, E.; Yusuf Yaman, M.; Saat, G.; Karadas, F.; Ülgüt, B.; Dag, Ö. Synthesis of Mesoporous $LiMn_2O_4$ and $LiMn_2-xCo_xO_4$ Thin Films Using the MASA Approach as Efficient Water Oxidation Electrocatalysts. *J. Mater. Chem. A* **2018**, *6*, 13925−13933.
(49) Karakaya, C.; Solati, N.; Savacı, U.; Keleş, E.; Turan, S.; Çelebi, S.; Kaya, S. Mesoporous Thin-Film NiS_2 as an Idealized Pre-Electrocatalyst for a Hydrogen Evolution Reaction. *ACS Catal.* **2020**, *10*, 15114−15122.
(50) Wienold, J.; Jentoft, R. E.; Ressler, T. Structural Investigation of the Thermal Decomposition of Ammonium Heptamolybdate by in Situ XAFS and XRD. *Eur. J. Inorg. Chem.* **2003**, *2003*, 1058−1071.
(51) Wang, H. W.; Skeldon, P.; Thompson, G. E. XPS Studies of MoS2 Formation from Ammonium Tetrathiomolybdate Solutions. *Surf. Coat. Technol.* **1997**, *91*, 200−207.
(52) Wu, L.; Wang, X.; Sun, Y.; Liu, Y.; Li, J. Flawed MoO_2 Belts Transformed from MoO_3 on a Graphene Template for the Hydrogen Evolution Reaction. *Nanoscale* **2015**, *7*, 7040−7044.
(53) Anantharaj, S.; Ede, S. R.; Sakthikumar, K.; Karthick, K.; Mishra, S.; Kundu, S. Recent Trends and Perspectives in Electrochemical Water Splitting with an Emphasis on Sulfide, Selenide, and Phosphide Catalysts of Fe, Co, and Ni: A Review. *ACS Catal.* **2016**, *6*, 8069−8097.
(54) Bockris, J. O.; Potter, E. C. The Mechanism of the Cathodic Hydrogen Evolution Reaction. *J. Electrochem. Soc.* **1952**, *99*, 169.
(55) Joyner, J.; Oliveira, E. F.; Yamaguchi, H.; Kato, K.; Vinod, S.; Galvao, D. S.; Salpekar, D.; Roy, S.; Martinez, U.; Tiwary, C. S.; Ozden, S.; Ajayan, P. M. Graphene Supported MoS2 Structures with High Defect Density for an Efficient HER Electrocatalysts. *ACS Appl. Mater. Interfaces* **2020**, *12*, 12629−12638.
(56) Ji, X.; Lin, Y.; Zeng, J.; Ren, Z.; Lin, Z.; Mu, Y.; Qiu, Y.; Yu, J. Graphene/MoS_2/$FeCoNi(OH)_x$ and Graphene/MoS_2/$FeCoNiP_x$ Multilayer-Stacked Vertical Nanosheets on Carbon Fibers for Highly Efficient Overall Water Splitting. *Nat. Commun.* **2021**, *12*, No. 1380.
(57) Mansingh, S.; Das, K. K.; Parida, K. HERs in an Acidic Medium over MoS_2 Nanosheets: From Fundamentals to Synthesis and the Recent Progress. *Sustainable Energy Fuels* **2021**, *5*, 1952−1987.

Downloaded from pubs.acs.org/aaemcq/article-pdf/5/6/7006/4453682/ae2c00640.pdf by KOC UNIV user on 29 October 2026

https://doi.org/10.1021/acsaem.2c00640
ACS Appl. Energy Mater. 2022, 5, 7006−7015